

Orbits Supporting Bars within Bars

Witold Maciejewski^{1,2} and Linda S. Sparke¹

¹*Department of Astronomy, University of Wisconsin, 475 N. Charter St., Madison, WI 53706*

²*Theoretical Physics, University of Oxford, Oxford, OX1 3NP, witold@thphys.ox.ac.uk*

13 November 2021

ABSTRACT

High-resolution observations of the inner regions of barred disk galaxies have revealed many asymmetrical, small-scale central features, some of which are best described as secondary bars. Because orbital timescales in the galaxy center are short, secondary bars are likely to be dynamically decoupled from the main kiloparsec-scale bars. Here, we show that regular orbits exist in such doubly-barred potentials and that they can support the bars in their motion. We find orbits in which particles remain on *loops*: closed curves which return to their original positions after two bars have come back to the same relative orientation. Stars trapped around stable loops could form the building blocks for a long-lived, doubly-barred galaxy. Using the loop representation, we can find which orbits support the bars in their motion, and what are the constraints on the sizes and shapes of self-consistent double bars. In particular, it appears that a long-lived secondary bar may exist only when an Inner Lindblad Resonance is present in the primary bar, and that it would not extend beyond this resonance.

Key words: celestial mechanics, stellar dynamics — galaxies: kinematics and dynamics — galaxies: nuclei — galaxies: spiral — galaxies: structure

1 INTRODUCTION

Recent high-resolution imaging, from space and from the ground, shows hitherto-unsuspected small-scale structures at the centers of many galaxies. In a number of barred galaxies, isophotal twists have been seen within the central few hundred parsecs. Small central bars, and occasional triply barred systems, are found: see Friedli (1996) for a review. The inner bars appear to be oriented randomly with respect to the larger bars (Buta & Crocker 1993), as expected if they are dynamically distinct subsystems. High-resolution CO maps of some disk galaxies show inner bars of molecular gas (*e.g.* Devereux *et al.* 1992, Benedict *et al.* 1996), but the presence of inner bars in infrared images (see *e.g.* Friedli *et al.* 1996; Jungwiert, Combes & Axon 1997; Mulchaey, Regan & Kundu 1997) suggests they contain old stars, and do not consist purely of young stars and gas. A high frequency of double bars is seen in a multicolor imaging survey of early-type barred galaxies recently completed by Erwin & Sparke (1999). The survey, performed with the WIYN telescope, and supplemented with archival HST images, covers a reasonably complete sample of 38 nearby ($z < 2000$ km/s), bright, barred S0 and Sa galaxies in the field. At least $\sim 20\%$ of these galaxies appear to possess secondary bars. In this paper, we will call the larger bar the *big*, *main*, *primary* or *outer* bar. The smaller bar will be referred to as the *small*, *secondary* or *inner* bar. Like Friedli (1996), we prefer to avoid the term ‘nuclear bar’, since a small bar on scales of tens or

hundreds of parsecs can exist even in the absence of a main kiloparsec-scale bar.

Within about 100 pc of a galactic center, orbital times are at least an order of magnitude less than those at a few kiloparsecs; thus a dynamically decoupled inner bar is likely to rotate faster than the outer structure. *The entire pattern is then not steady in any reference frame.* Such decoupled secondary bars have been seen to form in numerical simulations involving gravitating particles together with dissipative ‘gas clouds’ (Friedli & Martinet 1993, Heller & Shlosman 1994, Combes 1994, Shaw *et al.* 1995). The only systematic study of the orbital dynamics in a double-bar is that of Pfenniger & Norman (1990); they explored a weakly dissipative form of the equations of motion for a particle in one double-bar potential, finding a limit cycle in the plane of the bars, and spheroidal strange attractors. Orbits in the doubly barred potential do not have a conserved integral of motion, and in principle they might all be chaotic, exploring large regions of phase space. If the orbits are mostly chaotic, it is unlikely that such a system could be *self-consistent*, so that the average density of all the stars on their orbits in the time-varying potential adds up exactly to what is needed to give rise to the potential in which they move.

How can potentials including two independently rotating bars maintain themselves as gravitating systems? What are the conditions under which a gravitationally self-consistent double-bar structure could exist? We approach these questions by considering particle orbits in models that

include two rigid bars rotating at two constant, incommensurable pattern speeds. Such models cannot be fully self-consistent; Louis & Gerhard (1988) have shown that two bars which make up a self-consistent system must distort slightly as they rotate through each other. Nevertheless, we are looking for density distributions that are most likely to be close to a self-consistent model, i.e. for those which support orbital families capable of hosting sets of particles that together recreate the assumed time-dependent density distribution. In our investigation we use the concept of the *loop* introduced by Maciejewski & Sparke (1997). We explore constraints on double-bars that could maintain a likely self-consistent structure.

The concept of the loop is presented in §2. In §3, we review the methods that we used to find and to follow loops numerically in a doubly barred potential. In §4, we describe our models for the density distribution in doubly barred galaxies, constructed on the basis of parameters derived from observations. Various examples of loop families are given in §5. In §6, we closely examine loops supporting a likely self-consistent model of a double bar. Limitations imposed by orbital structure on self-consistent doubly barred systems, and their implications for gas flows, are discussed in §7. We summarize our results in §8. Analytical techniques that allow us to approximate the loops supporting a doubly barred density distribution, and to model the gas streamlines, are presented in Appendix A. In Appendix B, we derive the formulae for a potential of a prolate Ferrers bar.

2 THE CONCEPT OF THE LOOP

A gravitational potential consisting of two concentric bisymmetric bars that are independently rotating is not stationary in any reference frame. Nevertheless, if the bars rotate in the same plane around their centers with angular velocities Ω_B , Ω_S , the potential pulsates with a frequency $\omega_p = 2(\Omega_S - \Omega_B)$ in the frame rotating with one of the bars (note that the factor 2 comes from bisymmetry).

In the stationary potential of a single bar, particles on a closed periodic orbit move along it, always staying on the same curve. Stable periodic orbits form “backbones” of a steady potential: nearby orbits are trapped around them. Orbits in a double-barred galaxy will generally not be closed in any uniformly rotating frame of reference, since particles there undergo two forcing actions with non-commensurable frequencies. We want to extend the definition of an orbit, in order to find closed curves which can similarly serve as backbones of a non-steady, doubly barred system. We postulate that these are curves which, when populated with particles moving in a doubly barred potential, will return to their original positions every time the bars come back to the same relative orientation. We call these curves *loops* — they are a generalization of the closed periodic orbit in a single bar (see Maciejewski & Sparke 1997). A particle that begins its orbit from a position along a given loop returns to another point on the same loop after the bars have realigned. Loops change their shape as the bars rotate through each other. Particles trapped around loops that stay aligned with the bars in their motion could build up a long-lived, self-consistent, doubly barred galaxy, in the same way as particles trapped near closed periodic orbits in a singly barred potential.

Although here applied to two rigid bars rotating with constant pattern speeds, this method works for any potential pulsating with a constant period. In particular, the two bars do not have to be rigid, or to rotate with constant pattern speeds.

3 METHODS

3.1 Formal statement of the loop problem

We consider a phase space \mathcal{S} , whose points are the coordinates and momenta of particles at a given time. Then we define the mapping $\mathcal{P}(\mathcal{S})$, which assigns to each point in \mathcal{S} the coordinates of the corresponding particle after integrating its motion for one relative period $T_p = 2\pi/\omega_p$ of the bars. This mapping $\mathcal{P}(\mathcal{S})$ can be applied repeatedly, leading to consecutive *iterated maps*. For each point A of the phase space \mathcal{S} , the $\mathcal{P}^n(A)$ is called the n^{th} *iterate* of this point. The set of all iterates of a given point is called *the orbit* of this point *under the mapping* $\mathcal{P}(\mathcal{S})$ (see *e.g.* Lichtenberg & Lieberman 1992). Thus defined, the orbits divide the phase space into non-overlapping invariant sets: no point can be on two distinct orbits.

A Hamiltonian system in N dimensions with a periodically varying potential can be written as an autonomous system (one with a time-independent potential) in $N + 1$ dimensions (see *e.g.* Lichtenberg & Lieberman 1992, Louis & Gerhard 1988). If we look only at orbits in the symmetry plane in which the bars rotate, our 2-D potential changing periodically with a fixed frequency is equivalent to a 3-D autonomous Hamiltonian system. Regular orbits in this 3-D system are those that behave as if they have 3 integrals of motion: they are confined to a 3-D hypersurface of the 6-D extended phase space of the autonomous system. Our iterative mapping suppresses the dimension corresponding to time, so the 3-D hypersurface of a regular orbit is represented by a 2-D set of points. Thus if a point A lies on a regular orbit in the double-bar system, its orbit under $\mathcal{P}(\mathcal{S})$ is a 2-dimensional hypersurface in the 4-D space. Chaotic orbits will occupy 3 or 4 dimensions. If a point in the phase space \mathcal{S} lies on an orbit which closes after N times the relative period, its orbit under the mapping $\mathcal{P}(\mathcal{S})$ will consist of a 0-dimensional set of N points.

What about a point $A \in \mathcal{S}$, whose iterates form a 1-D curve? This point is not on a periodic orbit (since these form a 0-dimensional set under $\mathcal{P}(\mathcal{S})$), but it corresponds to a particle moving on a special kind of a regular orbit (those are only confined to 2-dimensional hypersurfaces). Every time the two bars return to the same relative position, the iterates $\mathcal{P}^n(A)$ always lie on this 1-D curve: we have a *loop* as defined in §2. A particle that starts from any position on the loop will in general return to another place on the same loop every time the bars align. Since no point can be on two distinct orbits, and since in general the iterates of one point on the loop fill the entire loop, every point $A(\mathbf{x}, \mathbf{v})$ which lies on a loop contains all the information about this loop.

In Figure 1a, we show how consecutive iterates of $A \in \mathcal{S}$ generate a loop in a doubly barred galaxy. Figure 1b shows 200, 400 and 4000 iterates $\mathcal{P}(\mathcal{S})$ for two points: the first lies near a stable loop, the second one does not. For the near-loop

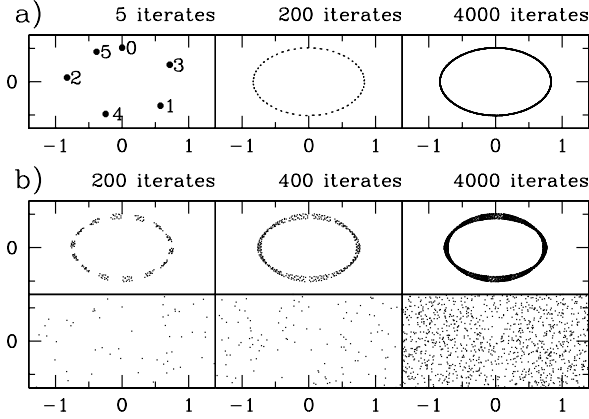


Figure 1. *a)* A loop in position space, generated by iterates of one of its points: 5 first iterates (left), 200 iterates (middle) and 4000 iterates (right). *b)* 200, 400 and 4000 iterates (left to right) in position space of a point that lies near a stable loop (top) and one that does not (bottom). Points are plotted when both bars are horizontal. The corresponding diagrams in the velocity space have the same appearance.

solution, the points are confined to a ring around the stable loop. Iterates of a typical point far from the loop quickly disperse, covering much of the phase space. Thus a stable loop can be found by adjusting the coordinates of point $A \in \mathcal{S}$, until its orbit under $\mathcal{P}(\mathcal{S})$ converges onto a 1-D closed curve. Unstable loops can only be found in this way if we have a very good guess at the starting conditions. Our method requires following a single particle for many bar rotations, and any particle starting close to an unstable loop will be lost by then. But since only stable loops can support the doubly barred systems, this is not a serious disadvantage. Another way to look at stability is to compare the ring widths for e.g. 100 and 200 iterations. They should be similar for a stable loop. For an unstable loop, a nearby particle moves away exponentially with time, increasing the width.

3.2 Numerical methods of finding the loop

To find iterates of point $A \in \mathcal{S}$, we follow a particle in the xy plane in a given potential $\Phi(\mathbf{x}, t)$, in which two bars rotate independently about the z -axis. We solve the equation of motion in a reference frame rotating with pattern speed Ω_B , which is equal to the angular speed of one of the bars. In the xy plane of the barred disk, $\Omega_B \perp \mathbf{r}$, and one can write the equation of motion (see *e.g.* formula 3-82 in Binney & Tremaine 1987) as

$$\ddot{\mathbf{r}} = -\nabla\Phi - 2(\Omega_B \times \dot{\mathbf{r}}) + |\Omega_B|^2 \mathbf{r}. \quad (1)$$

In Cartesian coordinates, it can be decomposed into its x and y parts:

$$\ddot{x} = -\frac{\partial\Phi}{\partial x} + 2\Omega_B\dot{y} + \Omega_B^2 x, \quad (2)$$

$$\ddot{y} = -\frac{\partial\Phi}{\partial y} - 2\Omega_B\dot{x} + \Omega_B^2 y. \quad (3)$$

We integrated the equations above using a variable-order, variable-step Adams integrating subroutine for first order

differential equations. This predictor-corrector method is well suited to our problem, for which we expect multiply periodic solutions. Under the forcing action of two bars, a particle can be given a kinetic energy large enough to escape. Any particle departing from the potential center to distances a few times larger than the extent of the outer bar was considered to be lost, and we looked only for loops in and around the bars.

We expect symmetric loops to be most important in symmetric bars. Therefore we restricted our search to the loops which are symmetric with respect to both x - and y -axes when the bars are aligned on the x -axis: we reflected the successive iterates $\mathcal{P}^n(A)$ about the two axes so that they occupy the $0 \leq \varphi < \pi/2$ region only. For symmetric loops the y -velocity on the y -axis is zero, and one can explore various initial x -velocities v_x for a given y -axis crossing coordinate y . To help us find the right v_x , we used the epicyclic approximation of Appendix A (see also Maciejewski & Sparke 1997). In general, consecutive iterates occupy the interior of a thick ring, but there is a range of v_x for which the ring generated by a particle starting at that point looks almost 1-dimensional. We assume that the real loop is nearby, and we need a practical definition of the loop: given $N(\mathbf{x}, \mathbf{v})$ pairs, we want to know if they lie on a 1-D curve. In principle this is not possible: there is a curve through any finite set of points. Nevertheless, we are looking for simple curves. The ideal choice might be to find the shortest line connecting the phase space positions of all the points, and to minimize its length as v_x varies. It is known though, that this task (the ‘traveling salesman problem’) is very expensive numerically: the number of operations needed to solve it grows exponentially with the number of points. Instead, we search for the loop by varying v_x in order to minimize the width of the ring in the xy plane formed by the iterates of the assumed starting point.

Before minimizing, we adjusted each loop candidate for flattening in the xy plane by finding the points with maximum x -coordinates x_{\max} and maximum y -coordinates y_{\max} . Then we rescaled the y -coordinates, multiplying them by y_{\max}/x_{\max} , to give a roughly circular ring. This was divided into 20 sectors, and the points with the smallest and largest radii were found in each sector. The difference of these extremal radii gives the width of the ring in each of the 20 sectors. We define the overall ring width $w(y, v_x)$ as the maximum width, or its average over the sectors. Now, we can minimize $w(y, v_x)$ with respect to the x -velocity and get the minimum width $w(y)$. Both minimizations proved to be useful, and the method itself is efficient and fast. In principle, we should be able to bring the ring width arbitrarily close to zero by increasing the number of iterates and sectors, and adjusting the initial velocity v_x . In practice, 20 sectors and 400 iterates proved to be good and efficient enough. A clear minimum is present at the same location for both estimates. We assume that the loop is generated by a particle with the starting x -velocity for which the width is minimal. The evolution of one loop thus defined is shown in Figure 2, together with the corresponding solution of the epicyclic approximation for comparison. The epicyclic approximation remains close to the real loop, which justifies using this approximation to begin the loop search. For non-symmetric loops, we would have to minimize with respect to 2 parameters; for example the initial values of v_x and v_y .

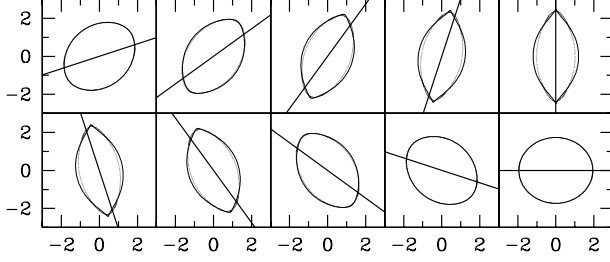


Figure 2. Evolution of a loop in Model 1 in the frame rotating with the main bar, which remains horizontal. The straight solid line marks the major axis of the small bar. The epicyclic approximation is plotted as a solid line, the true loop is dotted. Units are in kiloparsec.

Iterates of a given point are not always spread uniformly around the ring, but sometimes collect into several distinct clumps. This happens when the frequency ω with which the particle circumnavigates the loop is almost commensurable with the potential oscillation frequency ω_p . If these frequencies remain close to a lower order resonance, the number of clumps is small, and there are few points outside the clumps. This may produce an additional spurious minimum in the average ring width, but the minimum is narrow and changes quickly with the starting y -coordinate when the whole loop family is examined (see below), so its character is easily recognized.

In a single bar, some of the periodic orbits are self-intersecting; we expect to find self-intersecting loops in double bars as well. Our method of minimizing the ring width only in position- or velocity-space obviously breaks down there. We could consider the loop in the 4-dimensional phase space, where it never intersects itself, at the cost of a considerably larger computational expense and less clear visual examination of the results. Alternatively, we can calculate the width for part of the ring only. For example, if the loop intersects itself on the x -axis, these regions can be excluded from the calculation of the width. This procedure proved to be very fast and robust, and has been used exclusively.

The epicyclic approximation provides at most one solution for the loops and orbits at a given guiding radius. Additional loops, not predicted by the epicyclic approximation, can be present and may be dynamically important in the system of two bars. The only way to find them is to search the phase space of the initial conditions (y, v_x) for the ring width $w(y, v_x)$ values. In the following sections, we call this procedure the phase plane search. Sets of points (y, v_x) with low w that group along continuous lines should indicate loop families: continuous functions $v_x(y)$ for a range of y and v_x . The larger the region of low w around the line marking a loop family, the more orbits such a loop family traps around itself, and thus the more useful ‘backbone’ for building the galaxy it is.

We searched for loop families by changing the initial value y on the y -axis, and then adjusting the velocity v_x , so that the new pair (y, v_x) generates another loop. By analogy with periodic orbits in a single bar, we call $v_x(y)$ the *characteristic curve* for a given family. In our search we noticed that the minimal width of the ring of iterates can some-

times be large, but the loop family preserves continuity. We therefore accepted some fairly shallow minima in the automatic loop search. Doing so could derail the search from one loop family to another, if they come close to one another in the phase space (y, v_x) . To clarify when the border between different families has been crossed, we searched for orbital families twice. Once we did it by following particles starting on the y -axis, when the bars were both aligned on the x -axis, as described above. We did a second search, starting the particle on the y -axis when the big bar was still on the x axis, but the small bar was perpendicular to it. If the search algorithm loses the loop, one can go back to the phase plane display: identifying the region where the loop was lost often helps to answer why it was lost. Examples of this procedure will be given in sections 5 and 6.

4 MODELS BASED ON OBSERVATIONS

4.1 The structure of the models

To minimize the number of free parameters characterizing our models, we followed Athanassoula (1992a) in adopting analytical forms for the various potential components. Our potential consists of a bulge, a disk and two bars. There is no halo: in these 2-dimensional calculations its contribution to the rotation curve is included in the disk potential. Mass can be distributed arbitrarily into spherical and disk-like components, as long as they together make a realistic rotation curve.

The volume density of the bulge is given by a modified Hubble profile

$$\rho(r) = \rho_b(1 + r^2/r_b^2)^{-1.5}. \quad (4)$$

It requires two free parameters: the bulge central density ρ_b and the characteristic radius r_b . The surface density of the disk is defined by a Kuzmin-Toomre profile (Kuzmin 1956; Toomre 1963)

$$\sigma(R) = \sigma_0(1 + R^2/R_0^2)^{-1.5}; \quad (5)$$

like the bulge, this requires two parameters: σ_0 and R_0 . Following Athanassoula, we adopted the Ferrers ellipsoid to describe both bars, with volume density

$$\rho(x, y, z) = \begin{cases} \rho_0(1 - m^2)^n & \text{if } m < 1 \\ 0 & \text{otherwise} \end{cases}, \quad (6)$$

where in Cartesian coordinates $m^2 = x^2/a^2 + y^2/b^2 + z^2/c^2$. Thus the isodensity surfaces of our bars are concentric ellipsoids of constant axis ratio, and each bar is described by 5 free parameters: the central density ρ_0 , the Ferrers exponent n , and 3 semi-axes. We adopt prolate bars, and will set $n = 2$, which reduces the number of free parameters to 3. A larger index n allows the higher derivatives of the potential to be continuous, which in turn reduces the fraction of chaotic orbits in the solution. If there are loops supporting doubly barred potentials, they are more likely to be found for bars with higher n . In Appendix B, we show how the potential of a prolate Ferrers bar can be obtained by reducing Pfenniger’s (1984) solution for a triaxial bar. Both bars rotate about the z -axis with respect to the inertial frame; their pattern speed, or equivalently the Lagrangian radius,

Table 1. 12 parameters for our double-barred galaxy models

	Model 1	Model 2
<i>disk parameters</i>		
$R_{\max} = \sqrt{2}R_0$	20 kpc	20 kpc
$v_{\max} = 2\sqrt{\pi GR_0\sigma_0}/3^{0.75}$	164 km s ⁻¹	164 km s ⁻¹
<i>bulge and bar parameters</i>		
total mass within 10 kpc M_{tot}	$5 \times 10^{10} M_{\odot}$	$5 \times 10^{10} M_{\odot}$
central density $\rho_b + \rho_{0B} + \rho_{0S}$	$1 \times 10^{10} M_{\odot} \text{ kpc}^{-3}$	$4.8 \times 10^{10} M_{\odot} \text{ kpc}^{-3}$
primary bar semimajor axis a_B	7 kpc	6 kpc
primary bar quadrupole moment Q_m	$2.25 \times 10^{10} M_{\odot} \text{ kpc}^2$	$4.5 \times 10^{10} M_{\odot} \text{ kpc}^2$
Lagrangian radius of the big bar	$1.2a_B$	$1.0a_B$
axial ratio of the primary bar a_B/b_B	2.5	2.5
axial ratio of the secondary bar a_S/b_S	2.5	2.0
ratio of bar semimajor axes a_S/a_B	0.6	0.2
ratio of bar masses M_S/M_B	0.6	0.15
pattern speed of the secondary bar Ω_S	42 km s ⁻¹ kpc ⁻¹	110 km s ⁻¹ kpc ⁻¹

constitutes a 4th free parameter for each bar in our case. Thus the whole system is modeled with 12 parameters.

The parameters for the two models considered in this paper are given in Table 1. The potentials of the bulge, disk, and the big bar are chosen on the basis of Athanassoula's (1992a) 'standard model', constructed by Wozniak (1991) from a set of potentials inferred from observations of 16 SB0 galaxies and one SBa. The disk parameters are the same as in Athanassoula's model. The parameters of the secondary bars were chosen on the basis of the observations listed in the next subsection. In Figure 3, we show the rotation curve, calculated from forces along major and minor axis of the bar at bars aligned, and the curve of $\Omega - \kappa/2$ in the azimuthally averaged potential for both models.

Model 1 was designed to explore how far the secondary bar can extend in a doubly barred potential. It is the same model as the one used by Maciejewski & Sparke (1997). The parameters of the axisymmetric part match Athanassoula's average observed values almost exactly. But the main bar is weaker than the observed average, although falling within the range found by Wozniak (1991).

In Model 2, the quadrupole moment of the primary bar, its Lagrangian radius, and its axial ratio are the same as in Athanassoula's model. Since we use $n=2$ Ferrers bars, whose density drops faster with radius than in the $n=1$ bar modeled by Athanassoula, we extended the main bar all the way to its Lagrangian radius at 6 kpc, so the mass distributions are roughly similar. We increased the total central density to a value twice than that in Athanassoula's model, so the secondary bar comes close to having an ILR (Fig. 3). Of the 16 galaxies in the Athanassoula & Wozniak sample (Wozniak 1991), only two have such a big maximum of the $\Omega - \kappa/2$ curve, but the other parameters for the axisymmetric part fit these observations well. Both bars are stronger here than in Model 1, though still weaker than Wozniak's observed average.

4.2 Observed parameters of doubly barred galaxies

Friedli (1996) reviews available observations of possible double bars and estimates their basic parameters. We follow his notation here, in which three parameters are defined:

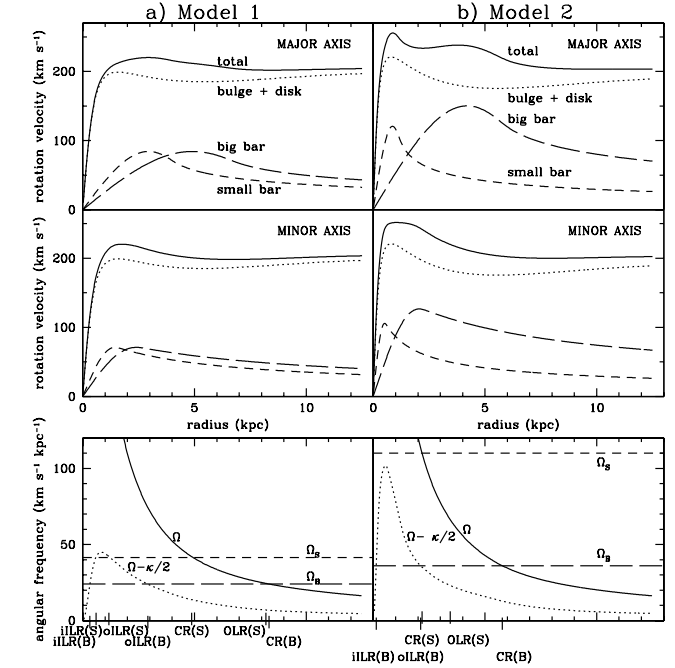


Figure 3. The rotation curve ($\sqrt{R d\Phi/dR}$) and its components along the major axis (top panels) and minor axis (central panels) for a) Model 1 and b) Model 2. The bottom panels show the angular frequency curves in the azimuthally averaged potential that determine the positions of resonances in the big bar (B) and small bar (S). We marked the inner and outer ILRs (iILR and oILR respectively), the corotation (CR), and the Outer Lindblad Resonance (OLR).

- (i) the maximum ellipticity in the barred region $e^{\max} = \max_a |1 - b/a|$, where a and b are the semimajor and semiminor axes of the fitted ellipses (note that this is the maximum ellipticity of the total light distribution, not of the bar only),
- (ii) the length ratio of the bars $\beta = l_B/l_S$, where l_B, l_S are the semi-major axes of the isophote ellipse fits at maximum or minimum ellipticity that corresponds to the main and secondary bar, respectively,
- (iii) the luminosity ratio of the bars $\gamma = L_B/L_S$: the ratio of total luminosities within the isophote of maximum (min-

Table 2. Observed parameters of doubly barred galaxies (Friedli 1996 / Mulchaey *et al.* 1997)

	average	min	max
β	7.2/4.9	3.7/1.83	18.0/8.8
γ	4.0/-	2.0/-	7.5/-
e_S^{\max}	0.34/0.30	-/0.2	-/0.43
e_B^{\max}	0.55/0.41	-/0.2	-/0.6

imum) ellipticity (note that thus defined, the inner bar’s luminosity is strongly influenced by the light from the bulge).

Wozniak *et al.* (1995) discuss how the last two parameters above depend on whether they are derived at minimum or maximum ellipticity. Mulchaey, Regan & Kundu (1997) present another, smaller but rather unbiased sample of doubly barred galaxies seen in K-band images. Average values at minimum ellipticity of parameters defined above for both samples (13 and 6 doubly barred galaxies respectively) are given in Table 2. There is an observational bias towards lower values of β and γ , because such systems are most easily found. Also e^{\max} for the small bar may be underestimated because of finite spatial resolution.

4.3 Model parameters versus observational constraints

To make a crude comparison between these models and the observed double bars, Erwin (1998, private communication) performed ellipse fitting on both our models in face-on position for a relative bar orientation of 60° , and derived the values of β , γ , e_S^{\max} and e_B^{\max} . Instead of surface brightness, the surface density was used. Since the contribution of the dark halo in our models is included in the disk mass distribution, the halo appears luminous here. It is not important though, since we are interested in the central parts of the galaxy, where the luminous matter is dominant. We calculate the luminosity of each bar as an integral over the interior of the ellipse with maximum or minimum ellipticity. We consider the parameters derived at the maximum ellipticity (max- e) to be better defined, because in real galaxies the radius of minimum ellipticity (min- e) at the main bar depends on the inclination angle. Table 3 gives the derived parameter values.

The β and γ parameters for Model 1 derived with both ‘min- e ’ and ‘max- e ’ methods are too small compared to the observed range (Table 2). Thus the secondary bar in Model 1 is too large; despite that, we explore this model to check if such a configuration is theoretically possible.

In Model 2, we see well defined ellipticity maxima, with a minimum between them. Note that both ‘max- e ’ and ‘min- e ’ methods give bar sizes smaller than the major axis of the Ferrers bar: in Model 2 the primary bar’s half-length is estimated to be 3.58 and 5.58 kpc respectively, when the semi-major axis of the Ferrers primary bar is 6.0 kpc. The measured values of the half-length of the secondary bar are 0.62 and 0.92 kpc respectively, when we set $a_S=1.2$ kpc. The β and γ parameters in ‘min- e ’ and ‘max- e ’ estimations have very similar values. Note that the mass in the inner parts of the galaxy is dominated by the bulge, and this makes γ

Table 3. Model parameters derived from isophote fitting

	Model 1		Model 2	
	min- e	max- e	min- e	max- e
β	3.07	1.98	6.08	5.79
γ	2.38	1.65	3.55	3.58
e_S^{\max}	0.118		0.159	
e_B^{\max}	0.182		0.428	

much smaller than the mass ratio of the bars. For Model 2, the β and γ values derived by the ellipse-fitting method correspond very well to the parameters in the observed samples (Table 2).

The only parameter of Model 2 that does not conform to the observed range, is the ‘measured’ maximum ellipticity of the secondary bar. This is only half as large as observed average, because the central parts of the model are dominated by our strong spherical bulge. It is very likely then, that distinct secondary bars are best observed against weak bulges, which cannot induce an ILR in them, unless the bars themselves are highly centrally concentrated.

From Figure 3 we see that the corotation of the secondary bar in Model 2 ($a_S=1.2$ kpc) is at 2.3 kpc, well outside the bar. Such a setup was forced after Model 1 failed to provide orbits supporting outer parts of the secondary bar — see the following section. The slowly rotating secondary bar seems to be consistent with the most successful numerical model by Friedli & Martinet (1993, Set II). They observe a secondary bar of 2.5 kpc size with corotation at 3.5 kpc, which makes $r_L/a \approx 1.4$, compared to 1.9 in our case. Thus the slowly rotating secondary bar appears to be justified by numerical models.

5 EXAMPLES OF LOOP SEARCH METHODS

5.1 Loop families in a single bar

To illustrate the methods which allow us to find loops in doubly barred galaxies, we show how the loop search is performed for a single bar. Here, we can choose arbitrarily the period of integration (we chose it to be very small) used to generate consecutive iterates of a given point. If this point lies on a periodic orbit, all its iterates will also lie on this orbit: in a single bar our loop finding technique locates the closed periodic orbits. If the orbit is stable, nearby particles should generate points populating a ring around this orbit.

We performed the search for Model 2, with the mass of the inner bar redistributed into the axisymmetric bulge, so that the central density and the total mass defined in Table 1 remain unchanged. Figure 4a illustrates the phase plane search defined in section 3.2. Two dark arches surround the main stable orbital families; in the notation of Contopoulos & Papayannopoulos (1980), these are the x_1 family, elongated parallel to the bar, and the x_2 family, oriented perpendicular to the bar. Thick dark arches, which overwhelmingly dominate the phase plane, mean that many quasi-periodic orbits are trapped around these periodic orbits. The unstable x_3 family is absent from this plot, because particles are not trapped around it.

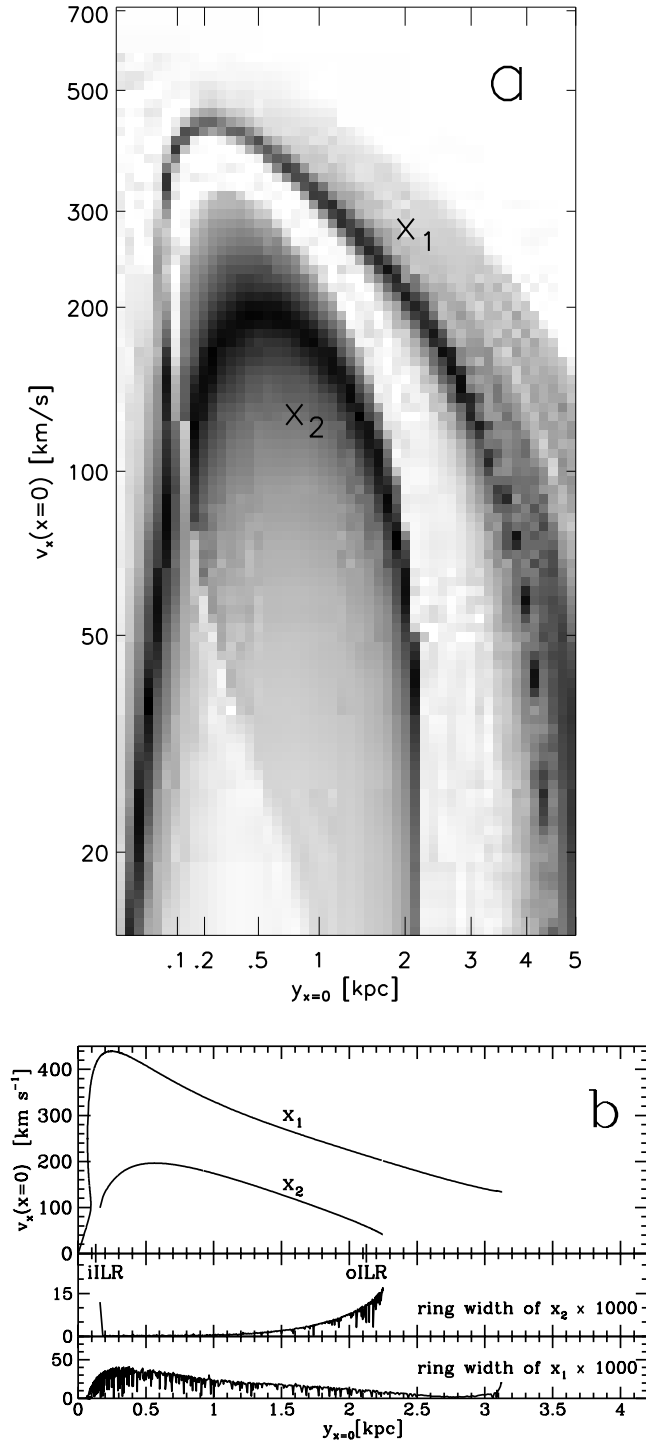


Figure 4. *a)* Phase plane search for particles in Model 2 without the secondary bar, which start on the minor axis of the bar. The colour reflects how strongly the first 400 iterates of a particle with given starting values (y, v_x) are confined to a 1-D curve. Darkest areas mark the near-loop solutions (smallest ring widths w). *b)* The characteristic curves for Model 2 without the secondary bar. The diagrams of minimal ring widths $w(y)$ along each family are attached.

The characteristic curves $v_x(y)$ for the x_1 and x_2 families are shown in Figure 4b, together with the minimum values of the ring width w defined in section 3.2, describing how close a set of iterates of the starting point given by (y, v_x) falls to a 1-D curve. The smooth appearance of the widths assures us that we follow a single loop family. In particular, when the orbital family x_2 disappears at large y , the ring widths increase rapidly. In §6, we will compare these orbits to the loops in the doubly barred Model 2, which is close to being self-consistent.

5.2 Loop families in a generic doubly barred potential: Model 1

Here we discuss the loop families in Model 1, the first of our doubly barred potentials. It is more general than Model 2, because the bars are not in mutual resonance, and the secondary bar is relatively large. Both bars are rapidly rotating: they extend to $\sim 85\%$ of their Lagrangian radii. To enable a comparison of the calculated loops to those from an epicyclic approximation, we made the bars weaker than in Athanassoula's (1992a) standard model. Both bars have two ILRs: those of the main bar are at 0.32 kpc and 2.9 kpc, and of the small bar at 0.6 kpc and 1.3 kpc.

Figure 5a presents a phase plane search for loops which are symmetric with respect to both x - and y -axes at the time when the bars are aligned on the x -axis. As in Figure 4a, two dark arches surround the stable loop families, though the top arch is broken in the middle. Extending the notation of orbital families, we call the loop family that corresponds to the x_2 orbital family of the main bar, the x_2 loop family. It appears clearly in Figure 5a, along with a wide dark stripe of near-loop solutions, which shows that particles can easily be trapped around this family. The x_1 loop family corresponds to the x_1 orbits in the outer bar. We see the inner part of the x_1 loop family clearly out to the radius where the bifurcation giving rise to the x_2 family takes place. The family abruptly discontinues above this point ($v_x \approx 250$ — when we refer to positions in $v_x(y)$ diagrams in this and the following sections, the length units are kpc, and the velocity units are km s^{-1}). The inner part of the x_1 loop family remains inside the inner ILR of the main bar. The x_1 loop family can be detected again for $0.4 < y < 2.0$, between the two ILRs of the main bar. But here it is not accompanied by a wide dark region of near-loop solutions, indicating that it may be not able to trap many particles around itself. Our plane search finds no clear x_1 loop family in the region $2 < y < 3$, close to the outer ILR of the main bar; there may be no loops there, or the resolution of our search may be too low — it shows only a grey region of near-loop solutions in this y range. For larger y this family is seen again, together with the accompanying dark grey band of near-loop solutions. The discontinuity of the x_1 family at large v_x seems to be common in our double-bar potentials; therefore we divide this family into an inner part x_{1i} inside the $v_x(y)$ maximum and an outer part x_{1o} outside it.

In addition to the x_1 and x_2 loop families, there is an interesting dark line marked in Figure 5a by A, which departs from the inner x_1 family in the lower left corner of the phase plane ($y \approx 0.13$, $v_x \approx 60$). It is examined separately below. No other loop families can be clearly seen in Figure 5a. In particular, there seem to be no stable loops corresponding

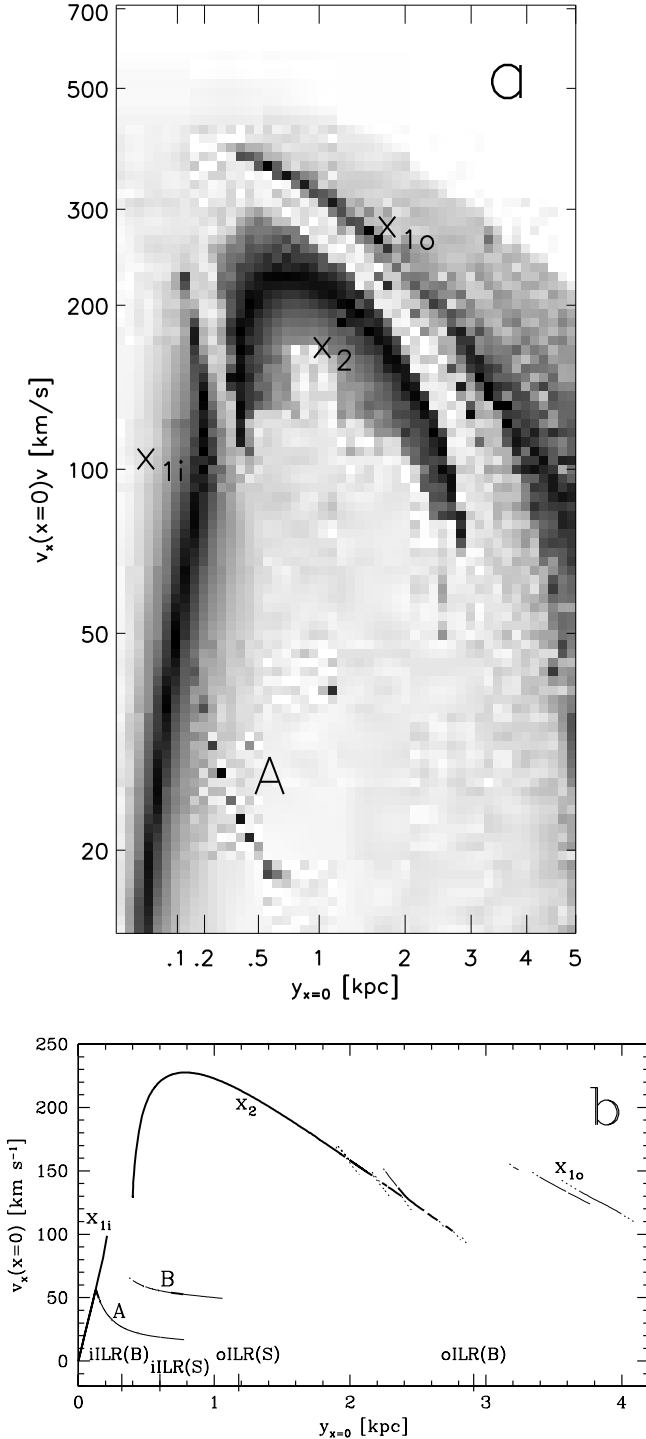


Figure 5. *a)* As Fig.4a, but for particles in Model 1, which start on the minor axis of the bar when the bars are aligned. *b)* The characteristic curves for Model 1. Loop families and resonances are labeled: x_{1i} and x_{1o} are the inner and outer parts of the x_1 family, as described in the text. The thickness of the line corresponds to the ring width: the loops with clear minima in width are represented by the thickest lines, the dotted lines mark areas where loops are no longer well defined. The labels A and B refer to loop families described in section 5.2.3

to x_2 orbits of the small bar, although this bar has a pretty wide zone between inner and outer ILRs.

All the loop families that we have found for Model 1 are displayed in Figure 5b; they are described in detail in the rest of this section. The thick lines correspond to well defined loops of small ring width; thin lines represent loops that are still well defined as single minima, but with considerable ring widths. The broken lines correspond to regions where loops were not well defined, mostly because at fixed y the ring width had multiple minima with v_x , or the minimum value of w was rapidly growing with y .

5.2.1 The x_2 loop family

We were able to follow the x_2 family as a continuous minimum of the ring width from $(y=0.4, v_x=130)$ to $(y=2.2, v_x=140)$, which remains inside the zone between inner and outer ILRs of the main bar. The x_2 loops still can be found in the range $2.2 < y < 2.8$, but the x_2 family is broken in this region. Our attempts to follow it fail, because multiple ring width minima compete with one another as y changes.

A representative set of the x_2 loops in the frame rotating with the primary bar is shown in Figure 6a. Here we confirm the hypothesis that we developed on the basis of the epicyclic approximation (Maciejewski & Sparke 1997): the outermost x_2 loops correspond to the x_2 orbits of the main bar and remain roughly perpendicular to it, while the inner loops of this family follow the secondary bar in their motion, and correspond to the x_1 orbits of the secondary bar. However, we cannot trace the x_2 loops all the way to the center, while the x_1 orbits of a single bar generally do extend to the center.

Throughout this paper we assume that our 2 bars are rigid and uniformly rotating. But the structure of the x_2 loops in Figure 6 tells us that it is a crude approximation only: the secondary bar, as outlined by its orbital (loop) structure, pulsates and accelerates as it moves through the main bar. The loops supporting the small bar are much thicker when it is parallel to the main bar: the minor axes of the inner loops are up to 1.8 times as large as when the bars are perpendicular. So if a secondary bar is self-consistently made out of particles trapped around these loops, then it should be thinner while perpendicular to the main bar. Also, the x_2 loops lead the small bar as it moves from the parallel to perpendicular position, and trail behind it when it moves back to align with the main bar. One can conclude that in a self-consistent model, the small bar should decelerate when going out of alignment with the main bar, and accelerate when on its way back to the aligned position. These conclusions will be confirmed by the loop structure of Model 2.

In Model 1, the x_2 loop family extends only to $x=2$ when the bars align on the x -axis, and only the loops extending roughly to $x=1.5$ there follow the small bar in its motion. But the secondary bar itself extends to $a_S=4.2$ kpc, so there are no loops which support the outer part of the secondary bar. By analogy with argument of Contopoulos & Papayannopoulos (1980) for the x_1 orbits in a single bar, we conclude that a self-consistent secondary bar cannot extend outwards beyond the region where the x_2 loops follow its motion relative to the large bar. The x_2 loops populate the region between the ILRs of the large bar. So we conclude that the major axis of the small bar is unlikely to be larger

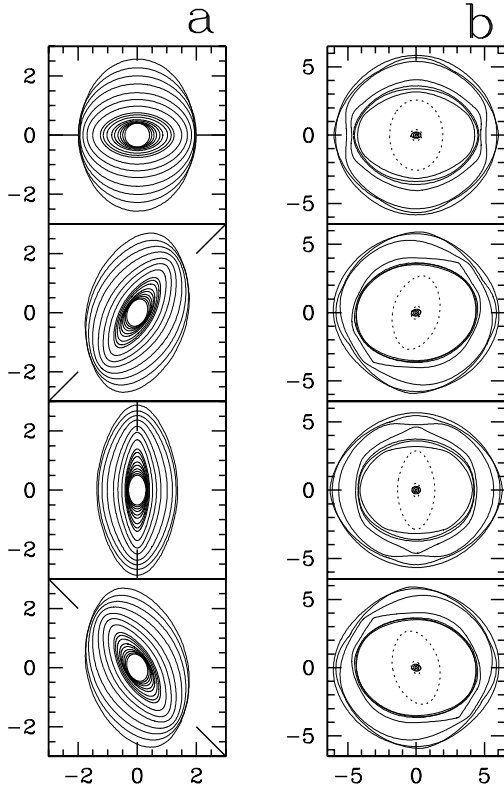


Figure 6. *a)* The x_2 loops in Model 1 in the rotating frame of the large bar, which remains horizontal. The straight lines at opposite sides or corners indicate the position angle of the small bar; time increases down the page. *b)* The x_1 loops at the same relative bar phases. The inner- and outermost x_2 loops are marked by dotted lines; three x_1 loops are displayed inside them. Units are in kpc.

than the outer extent of the x_2 orbital family of its main bar host along its major axis, unless the strength of the secondary bar relative to the main one is large enough to cause major changes in the loop structure.

5.2.2 The x_1 loops

The inner x_1 loops (the x_{1i} subfamily) show a very regular behavior in Figure 5a, where they are seen as a thick line in the lower left corner. The $v_x(y)$ curve is continuous throughout the whole region where these loops were detected: from the very center of the potential to $y=0.223$. At this y , the x -velocity increases rapidly with y and the loop family is lost in Figure 5a. The x_{1i} loops are almost circular and are represented by three innermost curves in Figure 6b.

Unlike the x_{1i} loops, loops belonging to the x_{1o} subfamily (outer x_1 loops) do not define a continuous function $v_x(y)$ in the plot of Figure 5b. The loop searching code repeatedly lost track of the minimum after covering only a short y range. For some y ranges, two comparably deep and wide minima were present, indicating that two loops exist at the same y but with different starting velocities v_x . The appearance of the x_{1o} loops is shown in Figure 6b. It is not regular, and these loops cover a very small part of the primary bar. Therefore it appears unlikely that the primary bar can be built in a self-consistent manner in Model 1.

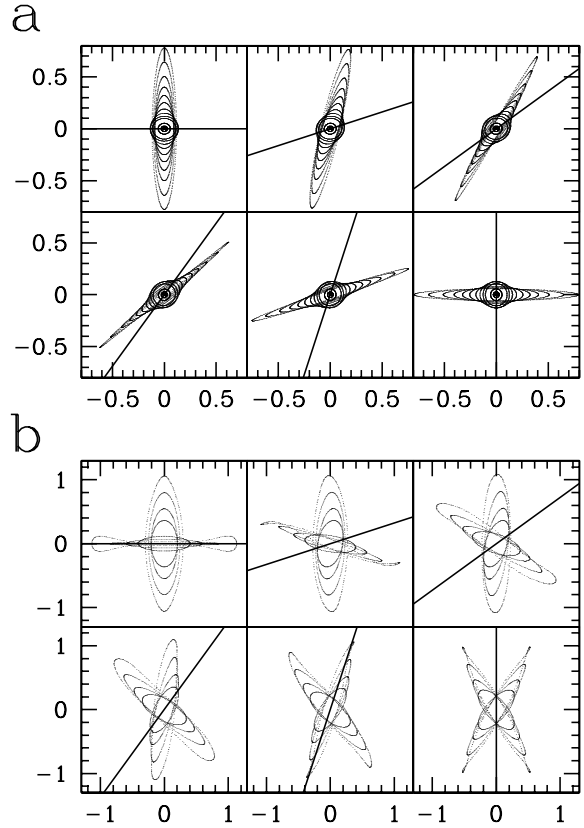


Figure 7. *a)* Evolution of the representatives of the loop family marked by *A* in Figure 5, displayed in the rotating frame of the large bar, which remains horizontal. The straight line indicates the position angle of the small bar. Only loops for the bars coming out of alignment are displayed: as the bars come back to alignment, the loops are mirror reflections of these. *b)* Representatives of the family marked by *B* in Figure 5 displayed in the same way as those in *a)*. Labels are in kpc.

5.2.3 Other loops

Although the secondary bar has an ILR, we found no loops corresponding to its x_2 orbits. Instead, we found a family of loops indicated by the set of dark pixels in Figure 5a (marked there by *A*), that departs to the right from the thick band marking the x_{1i} loops. Although this family is not surrounded by a dark band of particles trapped around these loops, the minimum ring width is well defined, and loops representative of this family are displayed in Figure 7a. When the two bars are aligned on the x -axis, the loops are perpendicular to them. But the loops precess in a sense opposite to the small bar, aligning with it when it makes an angle $\pi/4$ with the main bar, and becoming perpendicular to the small bar again when it in turn is perpendicular to the main bar. Thus the figure of the loop moves retrograde, but loop particles remain on prograde orbits with respect to either bar. The inner loops become rounder, and this family joins the x_{1i} loops at the point $y=0.13$, $v_x=57$ (Fig. 5b). This family obviously does not correspond to the x_2 orbital family in the small bar, and it does not support either bar. Nevertheless, it is consistently present in further modifications of Model 1, and in Model 2 described below.

Just as we can have multiply periodic orbits in a single bar, we can have higher order loops in double bars. If particles come back to the same curve only every other bar alignment, then after an odd number of alignments they lie along one curve, and after an even number, on another curve. Thus a single particle generates two closed curves in this case. One can easily extend this to N curves generated by a single particle returning to the same curve after every N alignments of the bars. We found many such higher order loop families in our search, one of which is presented in Figure 7b: both curves constituting each loop there precess retrograde, with a period twice the relative period of the two bars. In Figure 5b, this family (marked by B) runs parallel to the abovementioned family, when the larger out of two y -axis crossing points is considered to be a loop generator. Obviously, this family does not support any bar, and it is very unlikely that any of the higher order loop families can do it. Although we expect that abundant and complex higher order loops are present, we did not search for them.

6 APPROACH TO A SELF-CONSISTENT DOUBLY BARRED MODEL

Louis & Gerhard (1988) have shown, and the previous section illustrates, that bars which make up a self-consistent double-bar system must distort slightly as they rotate through each other. Thus our assumed potential, with two rigidly rotating bars, cannot be fully self-consistent. Here we are looking only for a model that may be close to being self-consistent, in which stable regular orbits give support to both bars in their motion. A real bar would have some chaotic orbits as well, which we do not consider here.

6.1 Choice of parameters leading to a nearly self-consistent model

A system similar to Model 1 could not be built in a self-consistent manner: its x_2 loops do not extend to the end of the secondary bar, and the x_1 loops cover only a small fraction of the primary bar. Making the secondary bar stronger may help to extend the x_2 family, but it would destroy the x_1 loops, which are already quite disrupted by the small bar in Model 1. A different solution has to be found.

First, we modified Model 1 by increasing the a/b axial ratio of both the bars from 2.5 to 4.0, while the product ab of the axis lengths remained constant. The x_1 loop family virtually disappeared, except for the inner x_{11} loops. The x_2 family broke into two well separated parts, and it may be difficult to support the secondary bar as well. On the basis of our limited search, weakness of the x_1 family seems to be a general feature of models with a relatively large, fast-rotating inner bar, like Model 1.

The new model, hereafter Model 2, is meant to be as close to Athanassoula's (1992a) standard model as possible. The quadruple moment of the primary bar is twice as large as in Model 1. From Model 1, we know that the secondary bar should not be too big. First we tried a long, but not massive ($a_S = 0.4a_B$, $M_S/M_B = 0.2$), secondary bar. The phase plane search showed that the x_1 family, which should support the longer bar, is practically absent for $y > 0.9$, while the bar length is $a_B = 6$. The x_2 family is broken into two parts,

both surrounded by regions of trapped semi-periodic orbits. This model may have a nearly self-consistent secondary bar, but cannot support the primary bar, and therefore has to be rejected.

Then we tried a smaller, but more massive secondary bar ($a_S = 0.2a_B$, $M_S/M_B = 0.3$). The loops from the x_1 family extend far enough in radius ($1.1 < y < 4$) to support part of the primary bar. The inner part of the x_1 family is quite extended, though: it suppresses the x_2 family, which in turn appears irregular and disrupted on the phase plane. In this model, part of the primary bar can be supported by loops, but the secondary bar is likely to be far from self-consistent.

The two attempts above suggest that our secondary bar is still too massive, or too large. Observations presented in §4 confirm this suspicion: the ratio of semimajor axes of the bars in the model, is beyond the observed range for our model with $a_S = 0.4a_B$, and at the lower end of the observed range for the model with $a_S = 0.2a_B$. Guided by the values listed in Table 2, we decided to make the secondary bar smaller and less massive. The ellipticity of the observed secondary bars is considerably smaller than that of the primary ones; therefore we set the axial ratio of the secondary bar at $b_S/a_S = 0.5$. The small bar is only 20% as long as the primary bar and has only 15% of the big bar's mass. Since in Model 1 the loops supporting the small bar failed to extend all the way to its corotation, in Model 2 we set the pattern speed so that the Lagrangian radius of the secondary bar is at $1.9a_S$. This also puts corotation of the small bar at the outer ILR of the big one, as suggested by Tagger *et al.* (1987).

6.2 Loop families supporting a nearly self-consistent Model 2

We constructed Model 2 with a particular interest in loops supporting the potential. We want to answer the question, is it possible to construct a model close to this one in a self-consistent way? Our first task is to survey the structure of x_1 and x_2 loop families, which we expect to support the primary and secondary bar, respectively. The results of the phase plane search for Model 2 are displayed in Figure 8a. Both x_1 and x_2 loop families are present there, with trapped orbits around them indicated by the dark areas. Note how similar this figure is to Figure 4a, in which a phase plane search for Model 2 with the main bar only was presented. Unlike in Model 1, this plane search suggests that both bars are likely to be supported by stable loops. Figure 8b shows the characteristic curves and the variation of minimum ring width $w(y)$ along each loop family. We find an additional loop family, marked there by b_T , supporting part of the main bar.

6.2.1 The x_2 family — loops supporting the small bar

We were able to find loops belonging to the x_2 family for $0.17 < y < 2.39$. Just before the x_2 family is lost at small y , the velocity drops rapidly. At the high- y end of the x_2 family, the ring widths increase making it harder to find the loop, before the loops disappear (Fig.8b). This family has two interesting features. First, around $y=0.406$, the characteristic

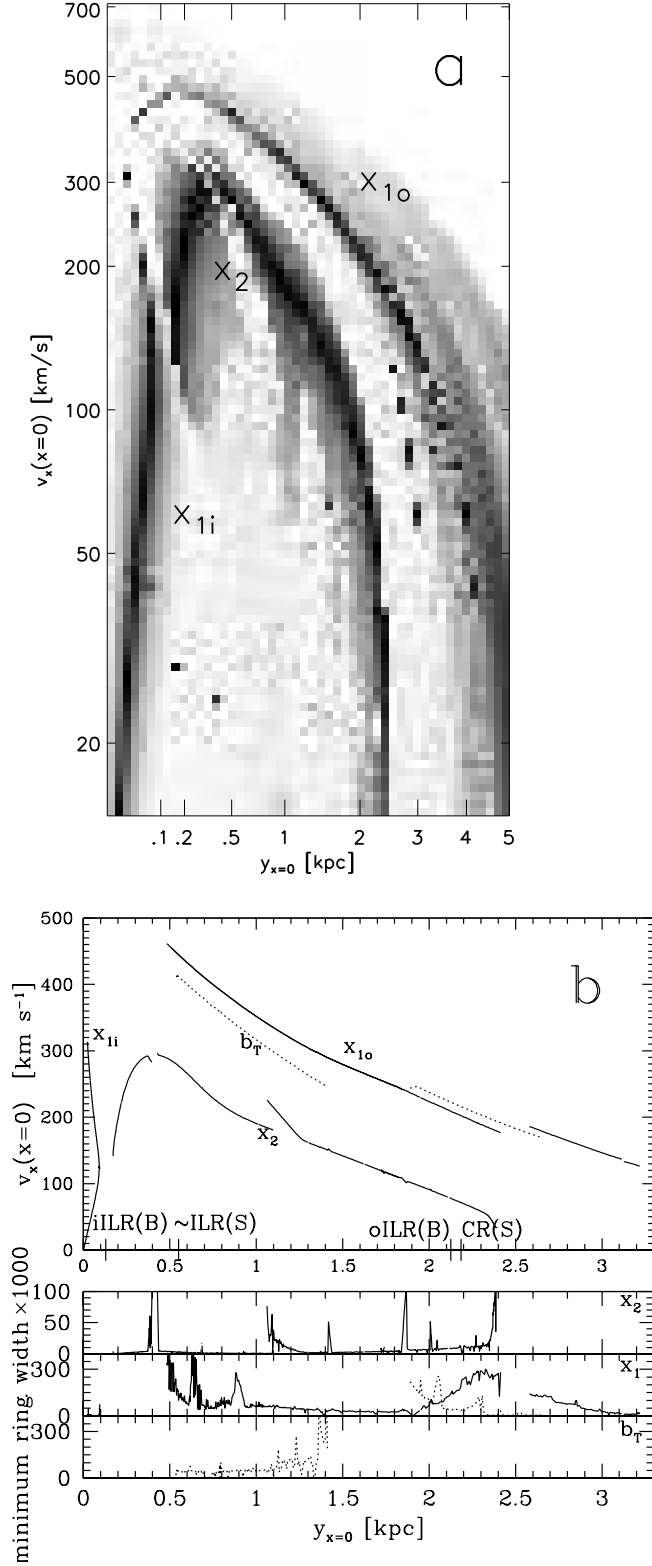


Figure 8. *a)* Phase plane search for Model 2 with two bars initially on the x -axis. *b)* The characteristic curves for Model 2 at bars aligned. The diagrams of minimal ring widths $w(y)$ along each family are attached. For clarity, some characteristic curves and the corresponding widths are marked in dotted. Note that the widths change much more abruptly with y than in Figure 4.

curve is discontinuous, and there is a small y range where no loops have been found. This corresponds to the white stripe crossing the x_2 arch in the phase plane search of Fig. 8a. The minimal ring width $w(y)$ increases steadily as this discontinuity is approached from both lower and higher y 's, before the width experiences a sudden jump. A detailed search for loops in this y range found no simple smooth invariant 1-D curve; but for a wide range of v_x , the particles are confined to well-defined rings. No higher order loops were detected in this region. It is possible that a similar small discontinuity occurs at $y=1.86$. Here, the ring width jumps an order of magnitude above its normal level over a narrow y -range, where we find no simple smooth 1-D curves. Again, for a wide v_x range we observe that the particles are confined to rings there.

At $y \approx 1.08$, the $v_x(y)$ curve for the x_2 loops splits in two; over a small range, there are two loops for each y value. The accompanying plot of ring widths shows that when approaching this region from higher y , the width of loops increases rapidly, and the searching code effectively loses the loop family. The minimum followed by our continuous search is no longer the global minimum, and another minimum is found which generates the continuation of this family to smaller y .

The overall appearance of the x_2 loops in Model 2 is presented in the central panels of Figure 9. The x_2 loops with $y \lesssim 0.5$ rotate with the small bar and extend out to about 0.85-0.9 of its semimajor axis. There the density in an $n=2$ Ferrers bar has dropped to 4% of its central value. Thus we conclude that the secondary bar is well supported by x_2 loops: even if the family breaks at $y = 0.4$, there are 'near-loop' solutions, and particles trapped around these can serve as the building blocks of the inner bar. Here we can also confirm our conclusion drawn on the basis of Model 1, that the secondary bar pulsates and accelerates, although these effects are smaller in Model 2.

6.2.2 Loops supporting the larger bar — the x_1 and b_T families

Figure 8b shows two disconnected parts of the x_1 family, which were detected with the search method described in section 3.2: the x_{1i} loops (inner x_1) at $y < 0.09$ and the x_{1o} loops (outer x_1) at $y > 0.5$.

The x_{1i} loops show a rapid growth in the x -velocity with y , and for $v_x > 120$, this loop family continues for decreasing y with velocities still growing. Therefore the x_{1i} loops are double-valued in this range. They cannot be traced beyond the point $v_x=310$, $y=0.024$, corresponding to a dark pixel in Figure 8a. We explore the question of connection between the inner and outer x_1 families later in this section.

The x_{1o} loops are not as well defined as the x_{1i} and x_2 loops — the minimum ring widths are larger. Near $y=0.65$ and 0.85, they rise to unacceptable values of 50% and 30% of the ring size, but no discontinuity in the loop family tracing is seen. We will return to this feature later in this section. In general, for the x_{1o} loops there is no clear single $w(v_x)$ minimum for a given y , but rather several less deep minima, of which one usually dominates. This is similar to what the x_2 loops experience near $y = 1.08$. For x_{1o} loops, two minima of roughly equal depth persist for the y range from 1.85 to 2.4, and are displayed as two parallel lines in Figure 8b. In

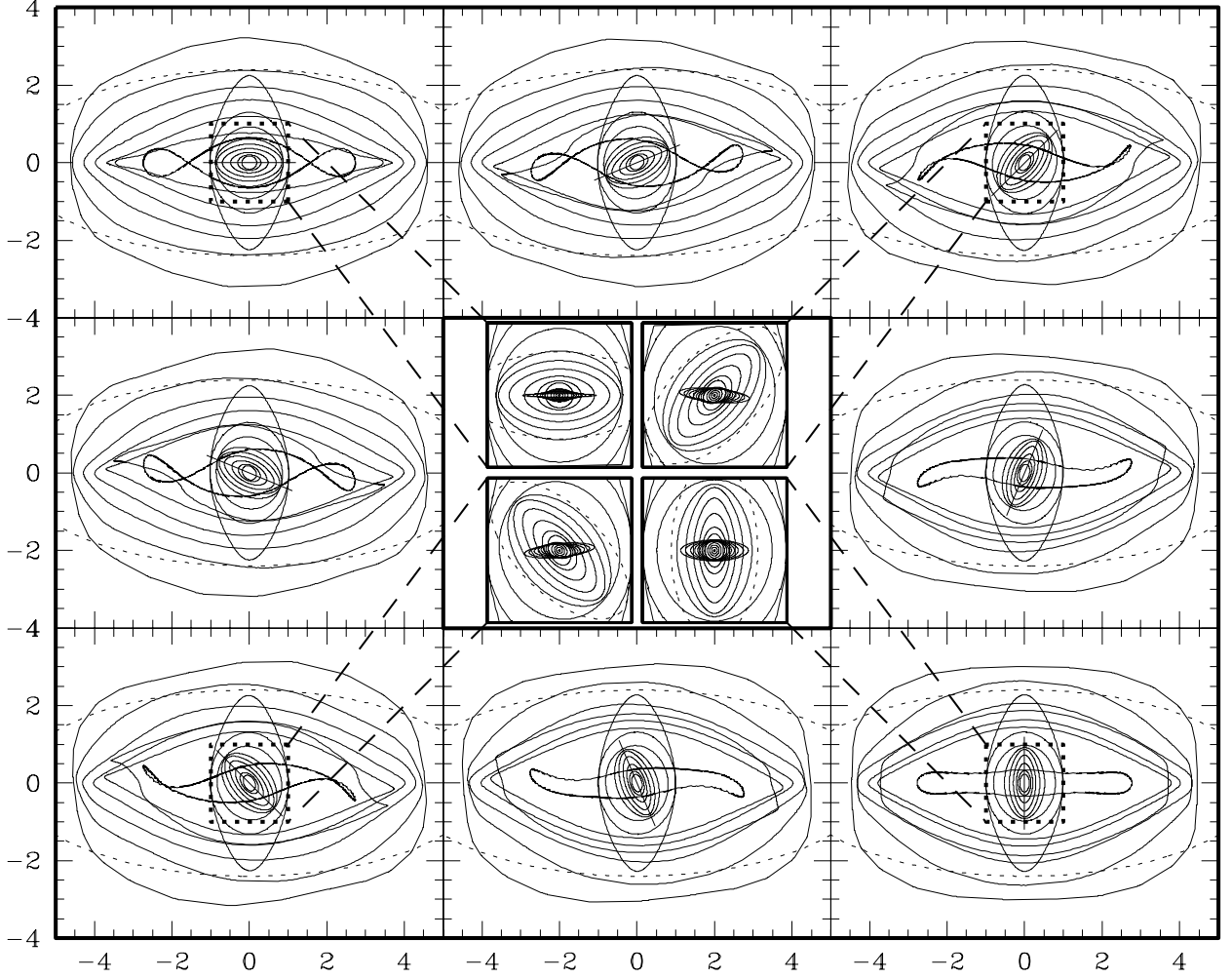


Figure 9. An overview of loops in a nearly self-consistent Model 2 of a doubly barred galaxy. The loops are displayed in the reference frame of the main bar at different relative positions of the bars. The outer bar is outlined by the dashed line and the major axis of the secondary bar is marked by a straight line on outer panels. The sequence follows along outer panels clockwise, with central regions magnified on inner panels, where the secondary bar is outlined by the dashed line. Units on the axes are in kiloparsec.

this region, the ring widths increase with y for the loops marked with a solid line, and this branch of the x_{10} loops is eventually lost at $y=2.4$. At that y , the widths on the other branch, marked with a dashed line, become small and behave in a very regular way. This branch is lost in turn at $y=2.65$. At $2.57 < y < 3.22$, another branch of the x_{10} loops exists; this is the branch extending to the highest y in Model 2. We consider the solid line extending from $y=0.5$ to 2.4 to be the main part of the x_{10} family, and we call the two abovementioned branches the x_{10} family additions.

The dotted line parallel to the x_{10} family and persisting for the y range from 0.54 to 1.4 (Fig. 8b), marks another loop family found in Model 2, which we name b_T for their 'bow-tie' appearance. Below 1 kpc, the ring widths for the b_T loops are smaller than those of the x_{10} loops, and the widths behave in a more regular way.

Figure 9 displays representatives of all loop families found for Model 2, as they change while the two bars rotate relative to each other. The two outermost loops belong to the two outer additions to the x_{10} family. The next four

loops inside them belong to the main part of the x_{10} family, and they undergo interesting oscillations when the two bars rotate through one another. The loop that is innermost when the bars are aligned (top left panel) develops cusps, and becomes much rounder: it ends up as a second outermost loop when the bars are orthogonal (bottom right panel). This leaves us with no x_{10} loops supporting the inner part of the main bar when the bars are orthogonal (bottom right panel). But there is one more loop inside the above mentioned set of four, which remains parallel to the main bar. It intersects itself at bars aligned, and belongs to the b_T family marked in Figure 8b by a dotted line. Loops from this family take a boxy shape at bars orthogonal and fill the central part of the main bar, thus supporting it in addition to the x_{10} loops.

The x_{11} loops are displayed against the x_2 loops in the 4 inner panels of Figure 9. The double-valued $v_x(y)$ curve for these loops means that when the two bars are aligned, two loops from this family cross the y -axis at the same point. One set of these loops is close to circular and can be detected

all the way to the potential center, the other one is elongated and gets longer with decreasing y , up to a semimajor axis of 0.5 kpc for $y=0.024$, where the family disappears. These narrow loops get stretched when the bars are orthogonal, but their semimajor axes roughly do not change, and they remain well aligned with the primary bar. Note that the x_{1i} loops are narrowest at bars aligned, unlike the x_2 loops which are narrower at bars orthogonal. Figure 9 also shows that in a potential of two independently rotating bars, sets of loops supporting the bars can penetrate through one another while each follows a different bar. If there are enough stars trapped on the x_{1i} loops, such a galaxy may appear as having a triple bar, with innermost and outermost bars aligned.

6.2.3 Loop search with bars orthogonal

One can get a more complete insight into the loop families in double bars by performing an additional search, with particles starting on the minor axis of the main bar (the y -axis), moving perpendicular to that axis, when the bars were orthogonal. Phase plane search of Figure 10a indicates both the x_1 loops (the upper arch) and x_2 loops (inner arch and plateau). A close-up of the upper arch is shown in Figure 10b: many bright strips running from the top-left to the bottom-right indicate areas where the iterates are no longer confined to a ring. The x_1 family is broken when they cross its dark arch. The structure at such intersections is similar to the features common in characteristic diagrams for orbits in a fixed potential, usually called the 4/1-like gaps (*e.g.* Contopoulos & Grosbøl 1989). It can be best seen at $y = 0.2$, $v_x = 460$ in Figure 10b. Around $y = 0.6$, there is a white strip which separates two dark strips: one surrounding the b_T family and originating at the top-left corner, and the other surrounding the x_{1o} loops originating on the right. It looks like this white strip overlaps with what would be an x_1 orbital family in a single bar there (see Fig. 4a), and it is unlikely that stable loops can be found there.

Comparing the loop families found with particles starting at the bars orthogonal with those found by the original search method earlier in this section allowed for a more complete picture of loops supporting the main bar. Figure 11 shows the characteristic diagrams for these loops, both at bars aligned and orthogonal. The x_{1o} loops, which occupied the region from 0.22 to 2.4 kpc in y at bars aligned, are compressed into a $1.4 < y < 2.8$ range at bars orthogonal. In this configuration, we find no x_{1o} loops at $y < 1.4$ to support the main bar. When the bars are orthogonal, at $1.4 < y < 2.2$ this family develops an interesting zig-zag on the characteristic curve (Fig.11b). It means that the innermost loops at bars aligned get pushed away at bars orthogonal and end up as the outermost ones. We gave an example of such a loop in section 6.2.2. On the diagonal of the ‘Z’ the trend reverses, and loops pulsate without changing their order. Eventually, the trend reverses again (the top of the ‘Z’); the loop which is outermost when the bars are aligned sinks inside, and is innermost at bars orthogonal. At the points ($y = 1.4$, $v_x^\perp = 308$) and ($y = 1.8$, $v_x^\perp = 250$), where the x_{1o} characteristic curve reverses, there is a set of rings that for a short range continues in the direction before reversing, but the ring widths increase rapidly.

In some regions of the lower branch of the ‘Z’ at bars orthogonal, loops do not transform to points on the x_{1o} charac-

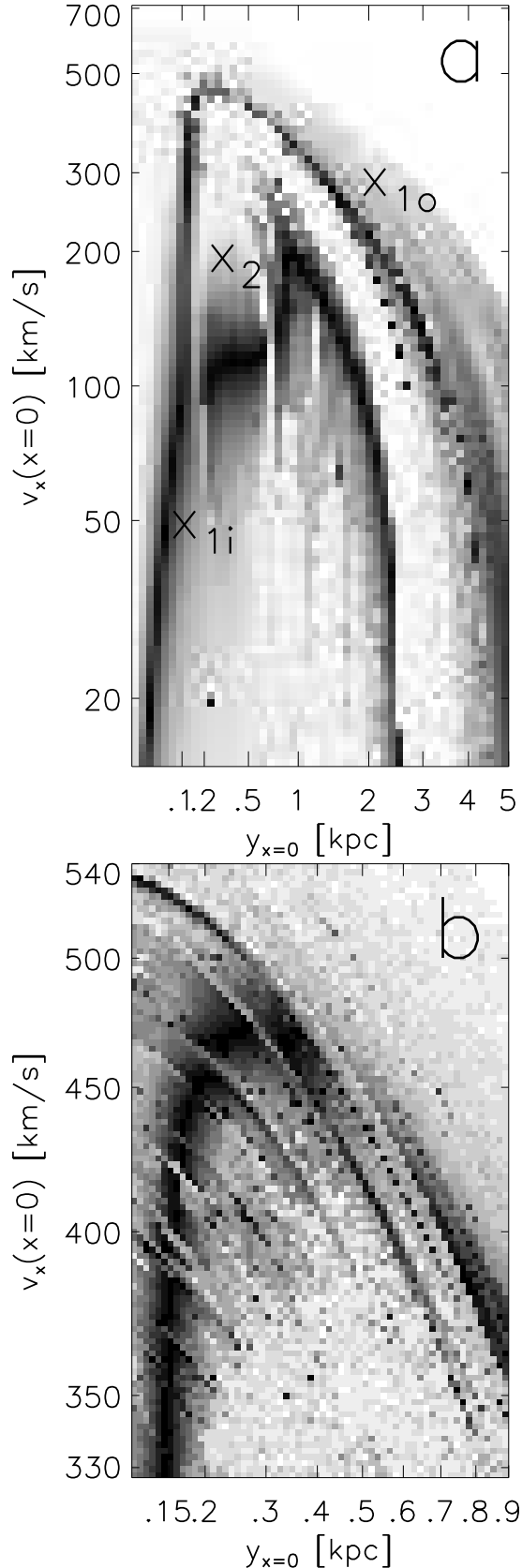


Figure 10. a) As Fig.8 but for a particle starting on the minor axis of the main bar when the bars are orthogonal. b) Close-up of the top of the ‘ x_1 arch’ from a).

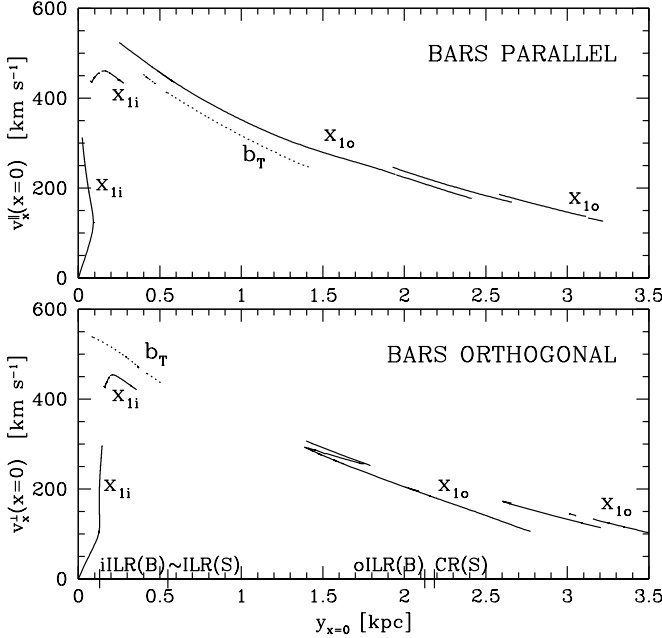


Figure 11. Two diagrams to compare the characteristic curves of loop families supporting the main bar in Model 2 at bars aligned (top) and orthogonal (bottom).

teristic curve at bars aligned monotonically, but get spread over a large y range. The transformed curve is disrupted at several places, which correspond to high ring widths for loops found at bars aligned (Fig.8b). Some real gaps in the stable loop families likely occur there, which are not just artifacts of our method. Thus the ‘high width’ found with our method may suggest that the loop sequence is broken and we may encounter part of a different family with a short stability range.

The b_T family and the two disconnected x_{1o} branches at high y in Figure 11a reverse order at bars orthogonal (the innermost loop becomes the outermost one). The two outer additions to the x_1 family may be connected by bridges similar to the diagonal of the ‘Z’ in the main x_{1o} subfamily: at $y = 2.6$, $v_x^\perp = 170$, the first addition to the x_{1o} loops changes order and aims towards the second addition, but we were not able to find a continuation for this set of loops.

We tried to find loops that could connect the x_{1i} and x_{1o} subfamilies. Our search at bars orthogonal resulted in finding loops represented by an arch at $y=0.2$, $v_x^\perp=450$ in Figure 11b. It may be a continuation of the x_{1i} subfamily extending to the galaxy center, but no connection of those two has been found. Several gaps in the ‘ x_1 arch’ there seen in the phase plane search (Fig.10b), suggest discontinuities in the x_1 family. The x_{1i} arch in Figure 11a most likely has no connection with x_{1o} loops either, since the b_T loop family seems to separate them.

6.2.4 Summary of loops supporting the main bar in Model 2

The main x_1 family in Model 2 consists of 2 subfamilies with some additions:

- (i) the inner x_{1i} subfamily originating at $(y = 0, v_x = 0)$,
- (ii) the addition to the inner x_{1i} loops marked by the arch in Figure 11,
- (iii) the main x_{1o} subfamily: there is no continuous transition from this subfamily to the x_{1i} subfamily,
- (iv) two outer additions to the x_{1o} subfamily.

There is an additional family, the b_T or bow-tie loops, but it still leaves a gap without a continuous set of simple stable loops for $0.5 < y < 1.4$ at bars orthogonal. There are some small loop subfamilies found at $0.7 < y < 1.5$ at bars orthogonal, but they are discontinuous. There are absolutely no loops at $0.5 < y < 0.7$ — there is a white strip of diverging iterates overlapping that part of the dark ‘ x_1 arch’ on the phase space diagram in Fig.10b.

In conclusion, we would say that the x_1 and b_T loops support most of the main bar at bars aligned. The x_{1o} loops are strongly influenced by the motion of the secondary bar. At bars orthogonal, they get rounder and group in the outer parts of the main bar. We were not able to find any x_1 loops supporting the inner part of the main bar when the secondary bar is perpendicular to it — the b_T loops fill up the center there, but a small gap between these two families remains (Fig.9). In section 6.2.1 we showed that the secondary bar is fully supported by the x_2 loops.

7 DISCUSSION, CONSEQUENCES FOR GAS FLOWS

The main goal of this work was to explore whether a galactic stellar disk with two non-equal bars rotating at different pattern speeds is dynamically possible. The ‘backbone’ for the orbital structure of this time-periodic system is provided by stable loops. These are closed curves, such that particles placed on them and moving in the potential of this system will return to the original curve after two bars have come back to the same relative orientation. A nearly self-consistent double bar should have stable loops elongated with each bar over appropriate radial range. In section 6, we gave an example of a doubly barred system where stable loops existed with the right shape, over the right range in radius, to support both the inner and the outer bars.

To create conditions most favorable to the existence of stable loops, we selected a smooth potential by choosing a high Ferrers index of the bars ($n = 2$). We also minimized the number of resonances by putting the corotation of the small bar at the outer ILR of the main bar. This overlapping of resonances, although not essential for the existence of self-consistent double bars, may be natural in dynamical systems (see Taggar *et al.* 1987). Our secondary bar was slow rotating, with corotation well beyond end of bar. To have the same resonant condition for a fast-rotating secondary bar, the inner bar would have to extend to the outer ILR of the main bar. In such a case, all the x_2 loops should follow the secondary bar in its motion, a configuration that we were not able to create. On the basis of our models, we believe that for double bars we may not be able to have both resonance overlapping and a secondary bar extending to its corotation.

The morphology of the gas flow in a barred potential strongly depends on the bar pattern speed. Straight shocks, often seen in large-scale bars, occur when the bar is rapidly

rotating, *i.e.* it extends at least to 80% of its corotation. For slower bars, the shocks curl around the bar and start forming a ring (Athanasoula 1992b). Thus in a slowly rotating secondary bar, we expect an elliptical flow to develop instead of straight shocks (Maciejewski 1999). The actual gas morphology will obviously be influenced by stars-gas interaction, self-gravity in the gas, and star formation processes, none of which is considered in this simple scenario.

8 SUMMARY

We have shown that doubly barred galaxy potentials allow stable regular orbits that can support the shape of both inner and outer bars. These multiply barred galaxies can be built as gravitationally self-consistent systems. In doubly barred galaxies, the most important loop families, which serve as their backbones, occupy the same parts of phase space as the x_1 and x_2 orbits in the single bar. The loop family corresponding to the x_1 orbital family in the main bar, always remains elongated along the main bar, even though the inner loops reside inside the secondary bar. The x_2 loop family, which at large radii behaves like the x_2 orbital family of the main bar, follows the secondary bar in its motion at smaller radii. No loop family corresponding to the x_2 orbital family in the secondary bar has been found.

Despite a limited number of models, we were able to draw conclusions about constraints that the orbital structure puts on the shapes, relative sizes and frequencies of the bars. The secondary bar can be supported by the x_2 loops which rotate smoothly with its figure. These loops change axial ratio as the bars rotate, and lead or trail the figure of the secondary bar, depending on the relative phase of the two bars. A self-consistent secondary bar, supported by stars trapped around these loops, must pulsate and accelerate as it revolves inside the main bar. Since the x_2 loops originate from the x_2 orbits in the potential of a larger bar, the size of a self-consistent secondary bar is approximately limited by the maximum extent of the x_2 orbits along the main bar's major axis. Because of these limitations, we were not able to find a self-consistent model of a doubly barred galaxy in which the secondary bar remains in resonant coupling with the main bar, and extends all the way to its corotation. Our nearly self-consistent model contains a slowly rotating secondary bar.

A strong secondary bar can easily disrupt the x_1 loops supporting the main bar; thus there are upper limits for the mass and size of the small bar. The inner region of the large bar can also be supported by another loop family, which we call the bow-tie or b_T family. The loops supporting one bar rotate through the ones supporting the other. Stars can be trapped around both these sets of loops, but gas can reside on at most one of them.

The concept of the loop developed in this paper provides a powerful tool to study particle orbits in any periodically pulsating gravitational potential: in double bars, pulsating spheres, and eccentric binaries. It is most promising in the last case: the motion of a massless test particle under the gravitational force of two point masses (the restricted three body problem), where only a few isolated closed orbits have been found so far.

ACKNOWLEDGMENTS

We thank Peter Erwin for useful discussions and help with fitting isophotes to our models. This research was supported by NSF Extragalactic Program grant AST93-20403 and by NASA Astrophysics Theory Program grant NAGW-2796.

REFERENCES

- Athanasoula, E. 1992a MNRAS 259, 328
- Athanasoula, E. 1992b MNRAS 259, 345
- Benedict, G.F., Smith, B.J. & Kenney, J.D. 1996 AJ 111, 1861
- Binney, J. & Tremaine, S. 1987 'Galactic Dynamics' (Princeton University Press)
- Buta, R. & Crocker, D.A. 1993 AJ 105, 1344
- Combes, F. 1994 in 'Mass Transfer Induced Activity in Galaxies', ed. I. Shlosman (Cambridge University Press), p170
- Contopoulos, G., & Grosbøl, P. 1989 A&AR 1, 261
- Contopoulos, G., & Papayannopoulos, Th. 1980 A&A 92, 33
- de Vaucouleurs, G. & Freeman, K.C. 1972 Vistas Astron. 14, 163
- Devereux, N.A., Kenney, J.D.P. & Young, J.S. 1992 AJ 103, 784
- Erwin, P. & Sparke, L.S. 1999 ApJ 521, L37
- Friedli, D. 1996 in 'Barred Galaxies', IAU Colloq 157, eds. R. Buta *et al.* ASP Conf. Ser., p378
- Friedli, D. & Martinet, L. 1993 AAp 272, 27
- Friedli, D., Wozniak, H., Rieke, M., Martinet, L. & Bratschi, P. 1996 AApS 118, 461
- Heller, C.H. & Shlosman, I. 1994 ApJ 424, 84
- Jungwiert, B., Combes, F. & Axon, D.J. 1997, A&AS 125, 479
- Kuzmin, G. 1956 Astron. Zh. 33, 27
- Lichtenberg, A.J., & Lieberman, M.A. 1992, Regular and Chaotic Dynamics, 2nd edition, (New York: Springer)
- Lindblad, P.O. & Lindblad, P.A.B. 1994 in 'The Physics of Gaseous and Stellar Disks of Galaxies', ed. I.R. King, ASP Conf Ser. Vol 66, p29
- Louis, P.D. & Gerhard, O.E. 1988 MNRAS 233, 337
- Maciejewski, W. 1999 in 'Galaxy Dynamics: from the Early Universe to the Present', 15th IAP Meeting, Paris 9-13 July 1999
- Maciejewski, W. & Sparke, L.S. 1997 ApJ 484, L117
- Mulchaey, J.S., Regan, M.W. & Kundu, A. 1997 ApJS 110, 299
- Perek, L. 1962 Adv. Astron. Astroph. 1, 65
- Pfenniger, D. 1984 AAp 134, 373
- Pfenniger, D. & Norman, C. 1990 ApJ 363, 391
- Sellwood, J.A. & Wilkinson, A. 1993 Rep. Prog. Phys. 56, 173
- Shaw, M.A., Axon, D., Probst, R. & Gatley, I. 1995 MNRAS 274, 369
- Tagger, M., Sygnet, J.F., Athanasoula, E., & Pellat, R. 1987 ApJ 318, L43
- Toomre, A. 1963 ApJ 138, 385
- Wada, K. 1994 PASJ 46, 165
- Wozniak, H. 1991 Ph.D. Thesis
- Wozniak, H., Friedli, D., Martinet L., Martin, P. & Bratschi, P. 1995 ApJ Supp 111, 115

APPENDIX A: LOOPS IN A WEAKLY BARRED POTENTIAL: THE EPICYCLIC SOLUTION

Here we show how approximations to loops can be found analytically within the epicyclic formalism. We also present the solution of a damped epicyclic approximation, which yields excellent approximation to the streamlines of gas flow in a singly-barred potential (Lindblad & Lindblad 1994, Wada 1994). The predictions for gas flow in doubly barred galaxies were explored by Maciejewski & Sparke (1997).

In the epicyclic approximation the motion of a test particle can be decomposed into the ‘guiding center’ motion, on a circle of radius R_0 with the angular velocity $\Omega(R_0)$ corresponding to circular motion in the axisymmetric potential Φ_0 , together with the epicyclic oscillations resulting from the forcing term Φ_1 , and a free oscillation at the local epicyclic frequency $\kappa(R_0)$. In a single bar, this formalism gives the approximate orbits that are the counterparts of the x_1 and x_2 families. On these closed orbits, the free oscillation is absent. In the same way, the solution of the epicyclic approximation in a double bar can lead to finding counterparts of the main loop families. We assume the free oscillation to be absent in the double bar as well. We extend the epicyclic solution for orbits in a barred potential (see *e.g.* Sellwood & Wilkinson 1993, Wada 1994 and Lindblad & Lindblad 1994) to double bars.

A1 The epicyclic solution for a Hamiltonian System

In planar polar coordinates (R, φ) the linearized equation of motion (1) yields following equations for R_1 and φ_1 first order corrections to the guiding center motion

$$\ddot{R}_1 + \left(\frac{\partial^2 \Phi_0}{\partial R^2} \Big|_{R_0} - \Omega_0^2 \right) R_1 - 2R_0 \Omega_0 \dot{\varphi}_1 = - \frac{\partial \Phi_1}{\partial R} \Big|_{R_0, \varphi_0}, \quad (\text{A1})$$

$$R_0^2 \ddot{\varphi}_1 + 2\dot{R}_1 R_0 \Omega_0 = - \frac{\partial \Phi_1}{\partial \varphi} \Big|_{R_0, \varphi_0}, \quad (\text{A2})$$

where $\Omega_0 = \Omega(R_0)$. If in addition to the main bar rotating rigidly with angular velocity Ω_B , there is another, secondary bar rotating with angular velocity Ω_S , the first order term Φ_1 in the multipole expansion of the potential in the frame of the main bar becomes time-dependent, and consists of two bisymmetric terms

$$\Phi_1(R, \varphi, t) = \Psi_B(R) \cos 2\varphi + \Psi_S(R) \cos(2\varphi - \omega_p t), \quad (\text{A3})$$

where $\omega_p = 2(\Omega_S - \Omega_B)$, and the time t was chosen such that $t = 0$ when bars are parallel. The first term on the right-hand side corresponds to the main bar, at rest in its own frame, and the second one describes the secondary bar, which rotates in this frame. After substituting $C_{B,S} = -(d\Psi_{B,S}/dr)|_{R_0}$ and $D_{B,S} = -(2\Psi_{B,S}/R)|_{R_0}$, the right-hand sides of equations (A1) and (A2), for radial and azimuthal motion respectively, become

$$- \frac{\partial \Phi_1}{\partial R} \Big|_{R_0, \varphi_0} = C_B \cos 2\varphi_0 + C_S \cos(2\varphi_0 - \omega_p t), \quad (\text{A4})$$

$$- \frac{1}{R_0} \frac{\partial \Phi_1}{\partial \varphi} \Big|_{R_0, \varphi_0} = -D_B \sin 2\varphi_0 - D_S \sin(2\varphi_0 - \omega_p t). \quad (\text{A5})$$

In general, we can start a particle orbit at any relative position of the bars, at an arbitrary time $t_s \neq 0$, with its guiding center at an arbitrary angle $\varphi_{0s} \equiv \varphi_0(t = t_s)$. The angle φ_0 of the epicycle center at a given time t is then $\varphi_0 = \varphi_{0s} + (t - t_s)\frac{\omega}{2}$, where $\omega \equiv 2(\Omega_0 - \Omega_B)$. The two bars induce two characteristic forcing frequencies, so we introduce two time counters, to integrate the equations of motion in a way analogous to Wada (1994). The first frequency is ω and the corresponding time t' is defined by $\omega t' = 2\varphi_0$. The second frequency is $\Delta\omega = \omega - \omega_p$ with the corresponding time defined by $\Delta\omega t'' = 2\varphi_0 - \omega_p t$. Equation (A2) for the azimuthal motion, with right-hand side stated explicitly in (A5), can be integrated over time to single out $\dot{\varphi}_1$ and substitute it back to equation (A1) for the radial motion. Thus we have the second order equation for R_1 in the doubly barred case

$$\ddot{R}_1 + \kappa^2 R_1 = \frac{m_B}{\omega} \cos \omega t' + \frac{m_S}{\Delta\omega} \cos \Delta\omega t'', \quad (\text{A6})$$

where $m_B = \omega C_B + 2D_B \Omega_0$, $m_S = \Delta\omega C_S + 2D_S \Omega_0$, κ is the free epicyclic frequency defined by $\kappa^2 \equiv 4\Omega_0(\Omega_0 - A)$, and A is the Oort constant. In equation (A6), one can substitute $R_1 = R_{1B} + R_{1S}$ and perform a standard separation of variables, which leads to two decoupled equations

$$\ddot{R}_{1B} + \kappa^2 R_{1B} = \frac{m_B}{\omega} \cos \omega t', \quad (\text{A7})$$

$$\ddot{R}_{1S} + \kappa^2 R_{1S} = \frac{m_S}{\Delta\omega} \cos \Delta\omega t'', \quad (\text{A8})$$

of the form exactly like Wada’s equation (4), the solution of which we already know. The steady-state solution for R_1 in a doubly barred potential consists then of two terms and can be written in the form

$$R_1 = -\frac{A_{0B}}{\omega} a_B \cos[2\varphi_{0s} + \omega(t - t_s)] - \frac{A_{0S}}{\Delta\omega} a_S \cos[2\varphi_{0s} + \omega(t - t_s) - \omega_p t], \quad (\text{A9})$$

where $A_{0B,0S} = 1/p_{B,S}^2$, $a_{B,S} = p_{B,S}m_{B,S}$, $p_B = \omega^2 - \kappa^2$, $p_S = \Delta\omega^2 - \kappa^2$. A similar solution can be written for φ . There is an obvious way to extend this method to the arbitrary number of N bars by performing a separation of N corresponding variables.

Clearly, the orbits in a potential of two independently rotating bars do not close. But from equation (A9) we can see that the time transformation $t \rightarrow t + 2\pi/\omega_p$ is equivalent to the initial angle transformation $\varphi_{0s} \rightarrow \varphi_{0s} + \pi\omega/\omega_p$. This means that after time $2\pi/\omega_p$, when the two bars return to the same relative orientation, the particle ends up at a place, which at the last time was occupied by another particle, with its guiding center at the same radius, but position angle differing by $\pi\frac{\omega}{\omega_p}$. Therefore particles having the same guiding radius interchange positions at consecutive bar alignments, while remaining on the curve appropriate to the guiding radius R_0 . This curve is the epicyclic approximation to *the loop*; in this linear approximation, a loop is a set of particles which have the same guiding radius, and lack any free epicyclic motion, but respond only to the periodic forcing of the two bars. A general orbit with that same guiding center will oscillate about the loop. Loops in the epicyclic approximation are presented for Model 1 in Maciejewski & Sparke (1997).

A2 The case of dissipative motion — the Damped Epicyclic Approximation

Lindblad & Lindblad (1994) and Wada (1994) showed that if a dissipative term is added to the equations of motion of a particle orbiting in a single rotating bar, the pattern of closed orbits in linearized solution closely reflects the gas streamlines in flows modeled hydrodynamically. This *Damped Epicyclic Approximation* gives us a cheap way to preview the hydrodynamic simulation. Obviously, this approach cannot reproduce a shock structure, or give the inflow rate.

Adding a friction term \mathbf{F}_{fric} to equation (1) we get

$$\ddot{\mathbf{r}} = -\nabla\Phi - 2(\boldsymbol{\Omega}_B \times \dot{\mathbf{r}}) + |\boldsymbol{\Omega}_B|^2 \mathbf{r} + \mathbf{F}_{\text{fric}}. \quad (\text{A10})$$

A true friction term \mathbf{F}_{fric} should be proportional to the velocity gradient in the gas, but this information is not available *a priori*, so we must use other forms of the dissipative term. We may postulate that the frictional force is proportional to the difference between the particle velocity $\dot{\mathbf{r}}$ and the circular velocity $\boldsymbol{\Omega} \times \mathbf{r}$ at its position in an axisymmetric potential Φ_0 , which is zero for a particle in circular orbit in that potential. The dissipative force \mathbf{F}_{fric} in the inertial frame can be written as

$$\mathbf{F}_{\text{fric}} = -2\lambda(\dot{\mathbf{r}}_i - \boldsymbol{\Omega} \times \mathbf{r}_i), \quad (\text{A11})$$

where \mathbf{r}_i is the particle's position in the inertial frame, and λ is the friction coefficient: the minus sign means that dissipation tends to reduce velocity deviations for positive λ . The friction described by Lindblad & Lindblad (1994) leads to this same expression for \mathbf{F}_{fric} , so we call this form the 'Lindblad friction'.

The rotation speed $\dot{\mathbf{r}}_i$ in the inertial frame is related to the speed $\dot{\mathbf{r}}$ in a frame rotating with the primary bar by $\dot{\mathbf{r}}_i = \dot{\mathbf{r}} + \boldsymbol{\Omega}_B \times \mathbf{r}_i$, thus equation (A11) becomes

$$\mathbf{F}_{\text{fric}} = -2\lambda[\dot{\mathbf{r}} - (\boldsymbol{\Omega} - \boldsymbol{\Omega}_B) \times \mathbf{r}]. \quad (\text{A12})$$

The bar pattern speed enters the friction formula because the dissipative term depends on both radial and tangential velocity deviations from the circular orbit. Wada (1994) used another form of friction, which depends on radial velocity deviations only:

$$\mathbf{F}_{\text{fric}} = -2\lambda(\dot{\mathbf{r}} \cdot \mathbf{r}) \cdot \mathbf{r}/|\mathbf{r}|^2. \quad (\text{A13})$$

In dissipative motion, the two components of particle velocity are coupled, which makes these two forms of friction compatible.

For Lindblad's friction, we get in a single bar the second order equation for the radial correction R_1

$$\ddot{R}_1 + 4\lambda\dot{R}_1 + 4(\Omega_0^2 + \lambda^2 - \Omega_0 A)R_1 = \frac{m}{\omega} \cos \omega t' + \frac{n}{\omega} \sin \omega t', \quad (\text{A14})$$

where t' is the same as defined for equation (A6), and $n = 2\lambda C$. When we use Wada's friction defined in equation (A13), the second order equation for R_1 takes the form

$$\ddot{R}_1 + 2\lambda\dot{R}_1 + 4\Omega_0 R_1(\Omega_0 - A) = \frac{m}{\omega} \cos \omega t'. \quad (\text{A15})$$

The epicyclic frequency κ depends on the friction strength for the Lindblad friction, but is the same as in the case with no friction when Wada's friction is used. The damping term is half as large for Wada's friction, which damps radial deviations only.

For Lindblad's friction, the dissipative counterpart of the second order differential equation (A6) for R_1 in the doubly barred case can be written as

$$\ddot{R}_1 + 4\lambda\dot{R}_1 + \kappa^2 R_1 = \frac{m_B}{\omega} \cos \omega t' + \frac{n_B}{\omega} \sin \omega t' + \frac{m_S}{\Delta\omega} \cos \Delta\omega t'' + \frac{n_S}{\Delta\omega} \sin \Delta\omega t'', \quad (\text{A16})$$

where the additional coefficients are $n_B = 2\lambda C_B$ and $n_S = 2\lambda C_S$. In presence of friction, we get the following steady-state solution for R_1 in a doubly barred potential

$$R_1 = -\frac{A_{0S}}{\Delta\omega} (a_S \cos[2\varphi_{0s} + \omega(t - t_s) - \omega_p t] + b_S \sin[2\varphi_{0s} + \omega(t - t_s) - \omega_p t]) \\ - \frac{A_{0B}}{\omega} (a_B \cos[2\varphi_{0s} + \omega(t - t_s)] + b_B \sin[2\varphi_{0s} + \omega(t - t_s)]), \quad (\text{A17})$$

where for a dissipative case $a_{B,S} = p_{B,SmB,S} + q_{B,SnB,S}$, $b_{B,S} = p_{B,SnB,S} - q_{B,SmB,S}$, $q_B = 4\lambda\omega$, and $q_S = 4\lambda\Delta\omega$. A corresponding solution can be written for φ . Like in the frictionless case, also in the damped epicyclic approximation particles with the same guiding radius remain on the same loops. These loops for Model 1 are presented in Maciejewski & Sparke (1997).

APPENDIX B: POTENTIAL OF A PROLATE FERRERS' BAR

Here we derive the potential of a prolate Ferrers' bar by reducing Pfenniger's (1984) solution for a triaxial bar. It can be expressed by a third order polynomial in x^2, y^2, z^2 with coefficients ω_{im} (the reduced version of Pfenniger's coefficients W_{ijk}) defined by

$$\omega_{im}(x, y, z) = \int_{\lambda}^{+\infty} \frac{du}{\sqrt{a^2 + u(b^2 + u)}} \frac{1}{(a^2 + u)^i} \frac{1}{(b^2 + u)^m} \quad (\text{B1})$$

The definition of λ , and $\Delta(\lambda)$ below, can be found in Pfenniger's paper (see also Binney & Tremaine 1987, pp. 57 and 61). Since $\lambda = 0$ inside the bar, ω 's do not depend on location there. Pfenniger's recurrence relations of (A11) type reduce to

$$\omega_{im} = (\omega_{i-1,m} - \omega_{i,m-1})/(a^2 - b^2). \quad (\text{B2})$$

with

$$\omega_{i0} = \frac{2}{2i-1} \left[\frac{1}{\Delta(\lambda)(a^2 + \lambda)^{(i-1)}} - \omega_{i-1,1} \right], \quad (\text{B3})$$

$$\omega_{0m} = \frac{1}{2m} \left[\frac{2}{\Delta(\lambda)(b^2 + \lambda)^{(m-1)}} - \omega_{1,m-1} \right], \quad (\text{B4})$$

$$\omega_{00} = \ln \left(\frac{1 + \sin \theta}{\cos \theta} \right) \frac{2}{\sqrt{a^2 - b^2}}, \quad (\text{B5})$$

$$\omega_{10} = \left[\ln \left(\frac{1 + \sin \theta}{\cos \theta} \right) - \sin \theta \right] \frac{2}{(a^2 - b^2)^{3/2}}, \quad (\text{B6})$$

$$\omega_{01} = \frac{\tan^2 \theta \sin \theta}{(a^2 - b^2)^{3/2}} - \omega_{10}/2, \quad (\text{B7})$$

where $\cos \theta = \sqrt{(b^2 + \lambda)/(a^2 + \lambda)}$. Then the potential of a prolate Ferrers bar can be written as

$$\begin{aligned} \Phi(x, y, z) = & -\frac{\rho_0 ab^2}{3} (\omega_{00} - 6x^2 y^2 z^2 \omega_{12} \\ & + x^2 \{x^2 [3\omega_{20} - x^2 \omega_{30}] + 3[y^2 (2\omega_{11} - y^2 \omega_{12} - x^2 \omega_{21}) - \omega_{10}]\} \\ & + y^2 \{y^2 [3\omega_{02} - y^2 \omega_{03}] + 3[z^2 (2\omega_{02} - z^2 \omega_{03} - y^2 \omega_{03}) - \omega_{01}]\} \\ & + z^2 \{z^2 [3\omega_{02} - z^2 \omega_{03}] + 3[x^2 (2\omega_{11} - x^2 \omega_{21} - z^2 \omega_{12}) - \omega_{01}]\}) \end{aligned} \quad (\text{B8})$$

The recipe above is equivalent to the formulae given by Perek (1962) and de Vaucouleurs & Freeman (1972).